RESEARCH ARTICLE

NANO · MICRO small
www.small-journal.com

Development of Double Fence Porphyrins as Self-Assembled Monolayers for Tin-Based Perovskite Solar Cells

Chun-Hsiao Kuan, Chi-Lun Mai, Velu Saravanan, Tsung-Chun Lin, Yun-Sheng Shih, Che-Hsin Kuo, Meng-Chen Tsai, Chen-Yu Yeh, and Eric Wei-Guang Diau**

The MC-series porphyrins, incorporating a variety of thiophene- and dithiophene-containing donor groups, offer an effective passivation strategy to eliminate Sn^{2+} defects on the surface of tin perovskite. Additionally, the C(15) position of the porphyrin core is linked to various electron-accepting groups, such as 2,1,3-benzothiadiazole, 4-(2,3-diphenylquinoxalin-5-yl)benzoic acid and an indacenodithiophene unit connected to carboxylic acid or cyanoacrylic acid. These groups act as self-assembled monolayers (SAMs) on indium tin oxide (ITO) substrates for tin-based perovskite solar cells (TPSCs). This study is the first example to report the use of porphyrin as SAM for TPSCs. In the presence of SAMs, the devices achieved efficiencies in the following order: MC-4 (8.65%) > MC-3 (6.19%) > MC-2 (5.06%) > MC-1 (5.03%). The outstanding performance of the MC-4 device is attributed to its retarded charge recombination, increased hole mobility, and superior hole-extraction capability. This approach offers a promising pathway for further developing porphyrin-based TPSCs.

1. Introduction

Porphyrin derivatives exhibit unique characteristics such as intense light absorption, superior charge transfer capabilities, and excellent thermal stability. The porphyrin structure, featuring eight β-positions and four *meso*-positions, is simple and easy to modify. Modifying the porphyrin structure can improve the efficiency of perovskite (PSK) solar cells (PSCs) through enhancements in photophysical, electrochemical, and charge-transport characteristics. Scientists are considering porphyrin's potential applications, such as defect passivation,[1–5] serving as hole-transporting materials (HTMs)[6–8] or self-assembled monolayers (SAMs) in PSCs,[9–11] exhibiting their multifunctional potential in PSC technology.[12,13] In recent years, Wei and co-workers have utilized a functional fullerene known as fullerene-porphyrin dyad (FPD), which consists of a porphyrin core to which three pentafluorophenyl groups are attached at the *meso*-positions C(5), C(10), and C(20). The *meso*-position C(15) is covalently bonded to a C_{60} fullerene moiety via a phenyl group and further functionalized with ester groups. The structural characteristics of FPD enable it to form chemical interactions with the perovskite lattice, enhancing the defect passivation effect and preventing the decomposition of perovskite under illumination. Consequently, devices based on FPD have achieved a power conversion efficiency (PCE) of 23% and significantly improved operational stability, with a T_{80} of over 1500 h.[14] In 2022, Zhang and co-workers introduced a novel D–π–A type zinc pyridine porphyrin derivative (ZnPP) as an additive for passivation through solvent processes, which is used to enhance perovskite film quality and achieve passivation of perovskite layers to reduce the amount of uncoordinated Pb^{2+}. The charge transfer loss caused by cations resulted in a high PCE (21.08%) and a high fill factor (82.91%) for the devices. They demonstrated the improved quality of perovskite thin films caused by the effective passivation of an optimized porphyrin structure. This study is of great significance for enhancing the performance and stability of perovskite solar cells.[1] In 2023, Yeh and co-workers introduced novel porphyrin derivatives (**AC-1**, **3**, and **5**) functionalized with carboxylic acid groups. These porphyrins serve as a structural framework connecting the ITO and the perovskite in inverted PSCs. The presence of electrons in porphyrins enhances the process of hole transfer and contributes to the development of SAMs, leading to a compact surface with fewer imperfections. The double-anchored **AC-3** and **5** served as SAMs on ITO effectively passivating the perovskite and improving the hole transfer ability. The champion

C.-H. Kuan, T.-C. Lin, Y.-S. Shih, C.-H. Kuo, E. W.-G. Diau
Department of Applied Chemistry and Institute of Molecular Science
National Yang Ming Chiao Tung University
1001 Ta-Hseuh Rd., Hsinchu 300093, Taiwan
E-mail: diau@nycu.edu.tw

C.-L. Mai, V. Saravanan, M.-C. Tsai, C.-Y. Yeh
Department of Chemistry
i-Center for Advanced Science and Technology (i-CAST)
and Innovation and Development Center of Sustainable Agriculture (IDCSA)
National Chung Hsing University
Taichung 402202, Taiwan
E-mail: cyyeh@dragon.nchu.edu.tw

E. W.-G. Diau
Center for Emergent Functional Matter Science
National Yang Ming Chiao Tung University
1001 Ta-Hseuh Rd., Hsinchu 300093, Taiwan

The ORCID identification number(s) for the author(s) of this article can be found under https://doi.org/10.1002/smll.202504259

DOI: 10.1002/smll.202504259

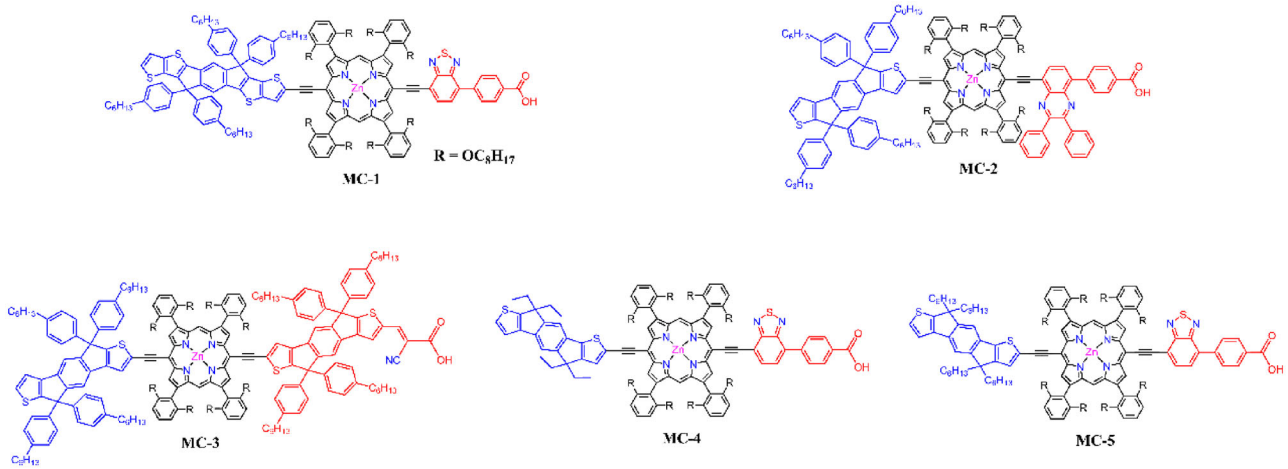

Figure 1. Molecular structures of **MC-1**, **MC-2**, **MC-3**, **MC-4**, and **MC-5** porphyrin dyes as HTMs for TPSC.

device using **AC-5** SAM achieves a PCE of 23.19% and a fill factor of 84.05%.[15]

In this study, we present four novel D–π–A porphyrin derivatives coded **MC-1**, **MC-2**, **MC-3**, **MC-4**, and **MC-5** (**Figure 1**) as SAMs for tin-based PSCs (TPSCs).[16] These porphyrin molecules play a crucial role in tuning the energy level of the electrode, optimizing charge injection and extraction, passivating surface defects, and minimizing charge recombination losses. Our design strategy involves the introduction of four β-phenyl rings to the porphyrin at the C(2), C(8), C(12), and C(18) positions, while incorporating two octyloxy groups at the *ortho*-position of each *meso*-phenyl ring to create a hydrophobic environment. This approach helps prevent molecular aggregation and improves the moisture resistance of the tin perovskite films. Photovoltaic performance data indicate that incorporating porphyrins from the **MC**-series at the C(5) position, along with a variety of donors, such as indacenodithienothiophene (IDTT) or indacenodithiophene (IDT) unit, effectively passivates Sn^{2+} defects on the PSK surface. Furthermore, the C(15) position of the porphyrin core is modified with various electron-accepting groups, such as 2,1,3-benzothiadiazole (BTD), 4-(2,3-diphenylquinoxalin-5-yl)benzoic acid, and an IDT unit attached to carboxylic and cyanoacrylic acids. Among these porphyrin SAMs, **MC-4** significantly improved the PCE by up to 8.65%. This research is the first example to highlight the considerable potential of porphyrins in enhancing the performance of TPSCs, representing a significant advancement in perovskite materials. **MC-4** and **MC-5** were both applied as self-assembled monolayers (SAMs) for interfacial modification in perovskite solar cells. While **MC-4** achieved the highest PCE of 8.62%, **MC-5** showed a marked performance decrease to 4.71% (Supporting Information).

2. Results and Discussion

These four D–π–A porphyrin derivatives **(MC-1-4)** feature a "double fence" architectural pattern, incorporating four β-phenyl rings anchored at the C(2), C(8), C(12), and C(18) positions of the porphyrin core. The phenyl rings are further functionalized with long-chain alkoxy substituents at the ortho-positions, which would enhance the hydrophobic barrier; the corresponding chemical structures are illustrated in Figure 1.

In the structures of **MC-1-4**, the porphyrin core at the C(5) position is covalently bonded to a conjugated backbone, which consists of an IDTT or IDT unit. This conjugation enhances charge mobility, a key factor for efficient charge transfer and improved device performance for TPSCs. The inherent thermal stability of the IDT backbone further boosts the durability of these organic semiconductors under various conditions, making them promising candidates as SAM molecules. It has been reported that using IDTT or IDT moiety can enhance the performance of organic photovoltaic devices, particularly in terms of PCE and stability.[17] Additionally, the incorporation of thiophene units within the structure optimizes charge carrier mobility and facilitates π-electron delocalization across the molecule.[18] The sulfur atoms within the thiophene rings of the IDTT and IDT frameworks play a vital role in passivating defects in perovskite materials (Sn^{2+} oxidation), which helps reduce non-radiative charge recombination.[19,20] On the opposite site of the donors, the C(15) position of the porphyrin core is linked to various electron-accepting groups, such as BTD, 4-(2,3-diphenylquinoxalin-5-yl)benzoic acid, and an IDT unit connected to carboxylic and cyanoacrylic acids. These groups can serve as anchoring groups for SAM, which are commonly used as hole transport layers in inverted p-i-n PSCs. Single-molecule thin films can be deposited on substrates like ITO, thereby enhancing device performance.

Scheme S1 illustrates the synthesis of double-fence zinc porphyrins **MC-1-4**. **MC-1** and **2**, involving Sonogashira coupling reaction. For **MC-1**, porphyrin (**1**) reacts with IDTT-Br **(2)** and BTD moiety (**3**) under catalytic conditions with $Pd_2(dba)_3$, $AsPh_3$, and NEt_3 in THF, yielding 33% of **MC-1**. Similarly, **MC-2** is obtained by reacting porphyrin (**1**) with the 2-bromo-4,4,9,9-tetrakis(4-hexyl/phenyl)-4,9-dihydro-s-indaceno[1,2-b:5,6-b"]dithiophene (**4**) and 4-(8-bromo-2,3-diphenylquinoxalin-5-yl)benzoic acid moiety (**5**) under similar conditions, yielding 38% of **MC-2**. For **MC-3**, the reaction involves porphyrins (**1**), (**4**) and 7-bromo-4,4,9,9-tetrakis(4-hexylphenyl)-4,9-dihydro-s-indaceno[1,2-b:5,6-b"]dithiophene-2-carbaldehyde (**6**) under similar catalytic conditions, producing 42.1% of **MC-3a**, which

Table 1. Electrochemical data for Porphyrin-Based materials HTMs, **MC-1-4**.[a)]

Sample	$E_{1/2}$(ox)[b)] [V]	$E_{1/2}$(ox) [V vs Fc]	$E_{1/2}$(red)[b)] [V]	$E_{1/2}$(red)[e)] [V vs Fc]	E_{HOMO}[c)] [eV]	E_{LUMO}[d)] [eV]
MC-1	0.828	0.1984	−1.149	−1.779	−5.298	−3.321
MC-2	0.813	0.183	−1.195	−1.825	−5.283	−3.275
MC-3	0.785	0.155	−1.217	−1.847	−4.945	−3.253
MC-4	0.807	0.177	−1.130	−1.760	−5.277	−3.340
MC-5	0.92	0.29	−1.144	−1.774	−5.390	−3.326

[a)] Redox potentials are measured in THF containing 0.1 M $[(n\text{-}Bu)_4N]PF_6$ as a supporting electrolyte. Potentials are quoted with Ag/AgCl reference electrode using ferrocene/ferrocenium (Fc/Fc^+) couple as internal standard; [b)] $E_{1/2}$(ox) and $E_{1/2}$(red) stand for oxidation and reduction potentials, respectively; [c)] The HOMO energy levels are calculated from first oxidation potentials (referenced to Fc/Fc^+) using the formula; [d)] E_{LUMO} is calculated similarly to E_{HOMO}; [e)] Irreversible process E_{pc}.

was then followed by Knoevenagel condensation, affording the final compound **MC-3** with a 36% yield. In the same way, **MC-4** and **MC-5** were synthesized using Sonogashira coupling, yielding 36% and 24%, respectively.[21,22]

Figure S1a presents the UV–Vis spectra of compounds **MC-1** to **MC-5**, highlighting distinct absorption peaks in both the Soret and Q bands. **MC-1** exhibits a Soret band at 489 nm and a Q band at 685 nm, consistent with the expected spectral features resulting from the IDTT group, which expands the π-conjugated system[23] **MC-2**, which incorporates 2,3-diphenylquinoline moieties, shows a Soret band at 484 nm and a split Q band with peaks at 636 and 679 nm. This slight blue shift is attributed to electron-withdrawing substituents, such as the benzoic acid group, which reduce the electron density on the quinoxaline benzene ring and enhance its electron-accepting ability.[24] **MC-3**, containing two IDT groups, displays a broadened Soret band ranging from 401 to 583 nm and a red-shifted Q band at 687 nm, indicative of enhanced conjugation provided by the IDT groups. **MC-4** exhibits a pronounced Soret band at 486 nm and a Q band at 686 nm. Lastly, **MC-5** shows a Soret band at 466 nm and a Q band at 630 nm, suggesting reduced conjugation compared to the other derivatives.

Cyclic voltammetry (CV) was employed to investigate the electrochemical properties of the compounds **MC-1-4** and determine their energy levels of the frontier orbitals. The experiments were carried out in tetrahydrofuran (THF), using 0.1 M tetrabutylammonium hexafluorophosphate ($TBAPF_6$) as the supporting electrolyte. The results are presented in Figure S1b and summarized in **Table 1**. From the CV data, the HOMO levels were estimated using the formula: $E_{HOMO} = -5.1 - (E_{1/2}(ox)$ vs $Fc/Fc^+)$. The HOMO levels of **MC-1** to **MC-5** were calculated to be −5.298, −5.283, −4.945, −5.277, and −5.390 eV, respectively. The corresponding LUMO levels were determined to be −3.321, −3.275, −3.253, −3.340, and −3.326 eV, respectively.

Density functional theory (DFT) calculations were performed at the B3LYP/6-31G(d) level of theory in THF to evaluate the effects of different redox moiety substitutions on the electronic properties of the **MC**-series molecules. These calculated molecular orbitals (MOs), illustrated in **Figure 2**, simulated the energy levels and frontier MOs of the compounds. For simplification, long alkyl and alkoxy chains in **MC-1-4** were replaced with methyl groups.

Figure 2 shows the distribution of the molecular orbital for the **MC** series, which represents alterations made to the corresponding porphyrin structures, highlighting changes made to the corresponding porphyrin structures. The optimized structures, aligned with red-shifted and broadened absorption spectra,

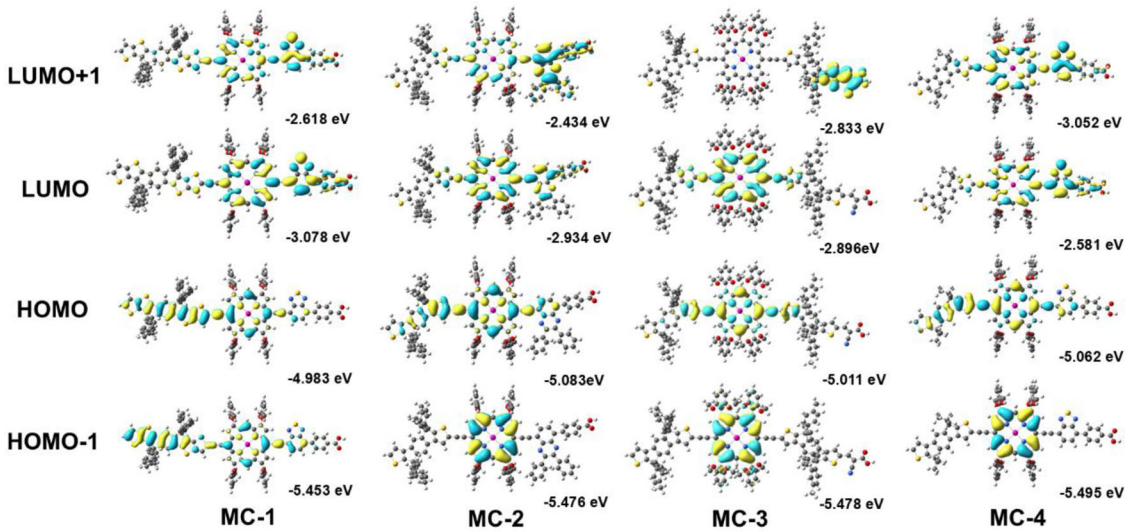

Figure 2. The energy level diagram and the corresponding molecular orbitals of double-fenced zinc porphyrin **MC-1-4** were calculated at the B3LYP/6-31G(d) level in THF. The methoxyl groups replace the long alkoxyl chains for simplicity.

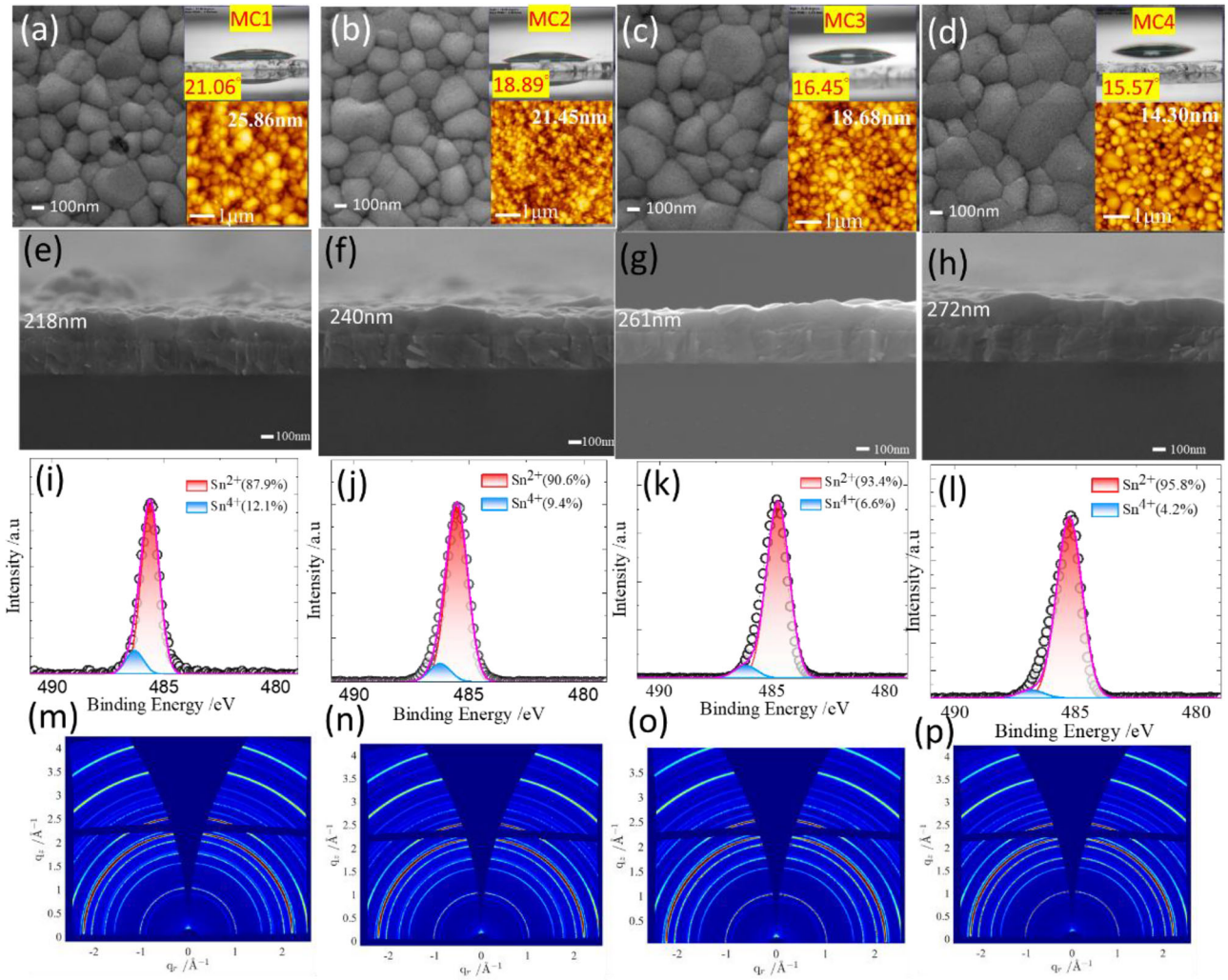

Figure 3. (a–d) Contact angles of SnI_2 on various porphyrins, along with top-view scanning electron microscopy(SEM) images and atomic force microscopy(AFM) images of the $FASnI_3$ on these porphyrins; (e–h) side-view SEM images of these perovskite films; (i–l) XPS analysis of tin perovskites fabricated on porphyrins' surfaces; (m–p) GIWAXS patterns.

demonstrate effective electronic interactions among the donor, porphyrin core, and acceptor groups via acetylene bridges. The highest occupied molecular orbital (HOMO) is primarily distributed in the electron-donating groups, with some contribution from carbon and nitrogen atoms within the porphyrins. In contrast, the lowest unoccupied molecular orbital (LUMO) is mainly localized in the acceptor regions, with BTD units having a greater influence than 4-(2,3-diphenylquinoxalin-5-yl)benzoic acid and IDT units. Notably, the introduction of IDTT in **MC-1** and IDT in **MC-4** leads to greater localization of the HOMO compared to IDT in **MC-2**, **MC-3**. Additionally, the increased overlap between the HOMO and LUMO in **MC-3** and **MC-1** is associated with their higher absorption coefficients, as observed by the UV–Vis spectra.[16,25]

The wetting behavior of various porphyrins is shown in **Figure** 3a–d. The contact angles for the SnI_2 precursor on porphyrin: 21.06° for **MC-1**, 18.89° for **MC-2**, 16.45° for **MC-3**, and 15.57° for **MC-4**. This surface modification greatly improves the FAI deposition, resulting in the $FASnI_3$ formation with the desired morphology. The connection between porphyrin and performance is evidenced by enhanced hydrophilicity and the effect of porphyrins on PCE. The morphologies of $FASnI_3$ deposited on different porphyrins were examined using SEM and AFM. Figure 3a–d also presents a top view of $FASnI_3$ deposited on different porphyrins. Among them, tin perovskite on porphyrin **MC-4** (Figure 3d) shows larger and more uniformly distributed grains compared to MC-1-3. This observation aligns with the AFM, which was used to assess the roughness of the $FASnI_3$ on different porphyrins. The investigation indicated that MC-4-based PSK exhibited reduced film roughness compared to the other PSKs. Figure S2 provides AFM and Kelvin Probe Force Microscopy (KPFM) of ITO/porphyrins. The roughness of ITO/porphyrins **MC-1-4** were measured to be 3.22, 3.40, 3.42, and 3.46 nm, respectively. The associated surface potentials were 2.64, 3.14, 2.64, and 2.47 mV, respectively. SEM cross-section images in Figure 3e–h depict the film thicknesses of perovskites **MC1-4**. Compared to the other films, the perovskite film of **MC-4** exhibited larger and more uniform

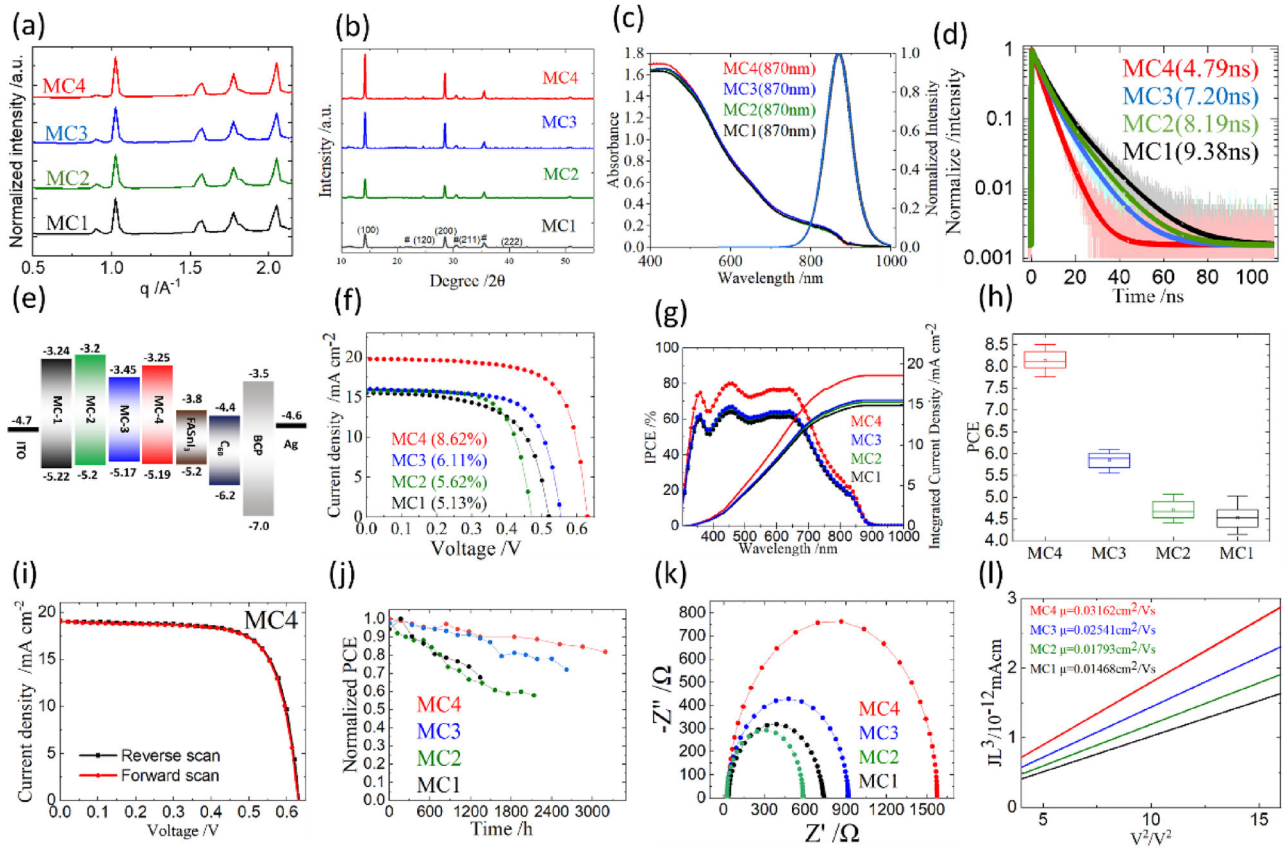

Figure 4. (a) Integrated intensity of grazing incidence wide-angle X-ray scattering (GIWAXS) and (b) XRD of $FASnI_3$ on different porphyrins; (c) UV–vis and Photoluminescence(PL) spectra and (d) time-correlated single-photon-counting(TCSPC) of $FASnI_3$ on various porphyrins; (e) the energy-level diagram for each porphyrin measured by UPS spectra; (f) the *J–V* curves; (g) IPCE spectra for devices made of **MC-1-4**; (h) boxplots of TPSCs for tin perovskite deposited on varied porphyrins as indicated; (i) effect of hysteresis of the **MC-1** device; (j) long-term performance stability of all devices stored in a glovebox; (k) EIS Nyquist plots for devices composed of $FASnI_3$ deposited on various porphyrins as indicated; (l) the space-charge limited current (SCLC) showing the hole mobilities (in $cm^2\ V^{-1}{\cdot}s^{-1}$) for **MC 1–4**.

grains. These observations align with the AFM results shown in Figure 3a–d.

Figure 3i–l shows the XPS Sn^{2+}/Sn^{4+} results for various porphyrin films as indicated. Functionalization of porphyrin significantly reduces the Sn^{2+}/Sn^{4+} oxidation, with the largest Sn^{2+}/Sn^{4+} ratio occurring on the **MC-4** sample (Sn^{2+}: 95.8%). The above analysis indicates that the **MC**-series porphyrins play an essential role in the subsequent growth of $FASnI_3$, for which **MC-4** gives the best quality of the perovskite film. A high-resolution GIWAXS (Figure 3m–p) of the **MC**-series film confirms their refined crystallinity and structured perovskite arrangement, which can enhance carrier transport and device performance. The integrated intensity of GIWAXS is shown in **Figure** 4a. The peak corresponding to tin perovskite was observed at around $q = 1.0$, while the separated SnI_2 from $FASnI_3$ appears at approximately $q = 0.9$. The $FASnI_3$ produced on **MC-4** exhibits a higher intensity with less intensity of the SnI_2 peak, suggesting its superior crystallization quality. The results are consistent with the XRD measurement, as depicted in Figure 4b. Moreover, we conducted measurements on the GIWAXS pictures of the **MC-1-4** samples at an incidence angle of a = 0.02°, with the results provided in Figure S3 of the Supporting Information. Evidence of π–π stacking was observed in the porphyrin film at q ≈1.6 $Å^{-1}$.

Figure 4c presents the UV–vis absorption and photoluminescence (PL) spectra of the four perovskite films, all of which exhibit similar band gaps and PL peak positions. Figure 4d shows the TCSPC experimental results, illustrating the temporal patterns of PL which can be fitted using a bi-exponential decay model. The fitted parameters for the data are detailed in Table S1. These results indicate that the hole-extraction rates of the porphyrins follow the following order: **MC-4** (4.79 ns) > **MC-3** (7.2 ns) > **MC-2** (8.19 ns) > **MC-1** (9.38 ns), suggesting that the **MC-4** porphyrin demonstrates the greatest hole-extraction ability. Figure 4e depicts the energy level diagram for all the components used in the construction of a TPSC device. The energy levels of the porphyrins were determined by analyzing the Ultraviolet Photoelectron Spectroscopy (UPS) data presented in Figure S4. The TPSC devices were constructed with a configuration ITO/porphyrin/perovskite/C60/BCP/Ag (Figure 4e). Figure 4f illustrates the *J–V* curves of porphyrin devices, with efficiencies showing the following order: **MC-4** (8.65%) > **MC-3** (6.19%) > **MC-2** (5.06%) > **MC-1** (5.03%). A detailed comparison of the relevant photovoltaic characteristics is provided in Table S2. In addition, we have synthesized **MC-5**, in which the two ethyl groups in **MC-4** are replaced with longer 4-hexyl- chains. This structural modification results in a significant performance

difference: **MC-4** achieves a PCE of 8.65%, whereas **MC-5** only reaches 4.71%. The IPCE spectra of the porphyrin devices are shown in Figure 4g, with the integrated current densities consistent with the *J–V* curves shown in Figure 4f. Twenty devices were manufactured for each porphyrin cell, with the performance boxplots displayed in Figure 4h and individual photovoltaic parameters summarized in Tables S3–S6 for devices **MC-1** to **MC-4**. Figure 4i shows the conventional forward and reverse scans of the **MC-4** device, confirming the absence of hysteresis. The long-term stability of the four devices stored in a glovebox under dark conditions is depicted in Figure 4j, with the **MC-4** device maintaining over 90% of its initial efficiency for >3000 h. Figure S5 demonstrates that the **MC-4** device when exposed to ambient air without encapsulation, retained over 85% efficiency for 5 h at the maximum power point (MPP) under continuous solar illumination.

To evaluate the superior performance of the **MC-4** device compared to others, we conducted electrochemical impedance spectroscopy (EIS) for all conditions under V_{OC} in the dark. The Nyquist plots shown in Figure 4k can be fitted by a single RC equivalent circuit model representing the extent of charge recombination. It reveals that the recombination resistance follows the order: **MC-4** > **MC-3** > **MC-1** > **MC-2**. This sequence correlates well with variations in V_{OC} and FF. Additionally, the charge mobility of the four porphyrin films was assessed based on space-charge-limited current (SCLC) (Figure 4l). Indicated that hole mobility follows the order: **MC-4** > **MC-3** > **MC-2** > **MC-1**, consistent with the overall performance shown in Figure 4f. Consequently, the outstanding performance of the **MC-4** device can be attributed to its reduced charge recombination (as indicated by EIS), outstanding hole mobility (as demonstrated by SCLC), and superior hole-extraction ability (as shown by TCSPC). The costs of the chemicals in synthesizing **MC-4** were estimated in Table S7 for comparison.

3. Conclusion

We have successfully developed a series of D–π–A porphyrin materials, coded as **MC-1-4**, and served as SAMs for TPSCs. Among these materials, **MC-4** can produce large and uniformly crystallized perovskite crystals, as observed in the SEM images. Additionally, AFM analysis shows that **MC-4** has the lowest root mean square (RMS) roughness value, indicating the smoothest surface and the most uniform crystallization of tin PSK. **MC-4** features an indene-thiophene functional group at the *meso*-5 position of the porphyrin ring, connected through an acetylene-bridged bond. Thiophene is known for its ability to passivate PSK surface to prevent tin oxidation, thereby reducing defect states, confirmed by the XPS measurements. Furthermore, the *meso*-15 position of the porphyrin ring was connected to BTD via an acetylene-bridged bond. The anchoring group chosen was a benzoic acid compound. Incorporating **MC-4** into the device has significantly increased PCE to 8.6%, which is much greater than the other porphyrin devices. This study presents the first example to demonstrate the considerable potential of porphyrins as SAM in enhancing the efficiency of lead-free perovskite solar cells, marking a promising concept for the future development of porphyrin SAMs for TPSCs.

Supporting Information

Supporting Information is available from the Wiley Online Library or from the author.

Acknowledgements

C.H.K. and C.L.M. contributed equally to this work. The author gratefully acknowledges the support of the National Science and Technology Council (NSTC), Taiwan (grant NSTC 112-2639-M-A49-001-ASP, NSTC 113-2639-M-A49-001-ASP, NSTC 110-2113-M-005-023, and NSTC 113-2113-M-005-017) and the Center for Emergent Functional Matter Science of National Yang-Ming Chiao Tung University (NYCU) and the Innovation and Development Center of Sustainable Agriculture of National Chung Hsing University (NCHU) from the Featured Areas Research Center Program within the framework of the Higher Education Sprout Project by the Ministry of Education (MOE) in Taiwan. The authors gratefully acknowledge Drs. Y.-W. Tsai and J.-M. Lin (TPS 25A1, NSRRC) for their valuable support in the analysis of GIWAXS data. We also extend our sincere thanks to Drs. B. H. Liu and C.-H. Wang (TLS 24A1, NSRRC) for their insightful guidance in interpreting the UPS and XPS measurements.

Conflict of Interest

The authors declare no conflict of interest.

Data Availability Statement

Research data are not shared.

Supporting Information

The Supporting Information is available free of charge:

Experimental methods, synthetic details, supplementary figures and tables for NMR, AFM/KPFM, GIWAXS, UPS and MPPT measurements.

Keywords

porphyrins, power conversion efficiency, self-assembly monolayer, solar Cells, tin perovskites

Received: April 7, 2025
Published online: May 28, 2025

[1] K. Su, W. Chen, Y. Huang, G. Yang, K. G. Brooks, B. Zhang, Y. Feng, M. K. Nazeeruddin, Y. Zhang, *Solar Rrl* **2022**, *6*, 2100964.
[2] Z. Guan, Z. Wei, F. Liu, L. Fu, N. Shan, Y. Zhao, Z. Huang, M. G. Humphrey, C. Zhang, *ACS Appl. Mater. Interfaces* **2023**, *15*, 51626.
[3] C. L. Mai, Q. Zhou, Q. Xiong, C. C. Chen, J. Xu, Z. Zhang, H. W. Lee, C. Y. Yeh, P. Gao, *Adv. Funct. Mater.* **2021**, *31*, 2007762.
[4] Z. Fang, L. Wang, X. Mu, B. Chen, Q. Xiong, W. D. Wang, J. Ding, P. Gao, Y. Wu, J. Cao, *J. Am. Chem. Soc* **2021**, *143*, 18989.
[5] T. A. Debele, B. Ojha, S. Kumar, Y. C. Chen, C. H. Hung, E. W. G Diau, *Solar RRL* **2024**, *8*, 2301084.
[6] D. Molina, J. Follana-Berná, *J. Mater. Chem. C* **2023**, *11*, 7885.
[7] C. L. Mai, Q. Xiong, X. Li, J. Y. Chen, J. Y. Chen, C. C. Chen, J. Xu, C. Liu, C. Y. Yeh, P. Gao, *Angew. Chem. Int. Ed.* **2022**, *134*, 202209365.
[8] M. J. Reis, A. T. Nogueira, A. Eulálio, N. M. Moura, J. Rodrigues, D. Ivanou, P. E. Abreu, M. R. P. Correia, M. G. Neves, Pereira, *Dalton Trans* **2023**, *52*, 14762.

[9] S. N. Afraj, C. H. Kuan, J. S. Lin, J. S. Ni, A. Velusamy, M. C. Chen, E. W. G. Diau, *Adv. Funct. Mater.* **2023**, *33*, 2213939.
[10] A. Abid, P. Rajamanickam, E. W. G. Diau, *Chem. Eng. J.* **2023**, *477*, 146755.
[11] C. H. Kuan, S. N. Afraj, Y. L. Huang, A. Velusamy, C. L. Liu, T. Y. Su, X. Jiang, J. M. Lin, M. C. Chen, E. W. G. Diau, *Angew. Chem. Int. Ed.* **2024**, *136*, 202407228.
[12] M. Urbani, G. de la Torre, M. K. Nazeeruddin, T. Torres, *Chem. Soc. Rev.* **2019**, *48*, 2738.
[13] K. Rakstys, C. Igci, M. K. Nazeeruddin, *Chem. Sci.* **2019**, *10*, 6748.
[14] Y. Liang, P. Song, H. Tian, C. Tian, W. Tian, Z. Nan, Y. Cai, P. Yang, C. Sun, J. Chen, *Adv. Funct. Mater.* **2022**, *32*, 2110139.
[15] C. M. Hung, C. L. Mai, C. C. Wu, B. H. Chen, C. H. Lu, C. C. Chu, M. C. Wang, S. D. Yang, H. C. Chen, C. Y. Yeh, *Angew. Chem. Int. Ed.* **2023**, *135*, 202309831.
[16] E. W. G Diau, E. Jokar, M. Rameez, *ACS Energy Lett* **2019**, *4*, 1930.
[17] E. Jokar, P. Y. Cheng, C. Y. Lin, S. Narra, S. Shahbazi, E. Wei-Guang Diau, *ACS Energy Lett* **2021**, *6*, 485.
[18] C. H. Kuan, J. M. Chih, Y. C. Chen, B. H. Liu, C. H. Wang, C. H. Hou, J. J. Shyue, E. W. G. Diau, *ACS Energy Lett* **2022**, *7*, 4436.
[19] C. H. Kuan, Y. C. Chen, S. Narra, C. F. Chang, Y. W. Tsai, J. M. Lin, G. R. Chen, E. W. G. Diau, *ACS Energy Lett* **2024**, *9*, 2351.
[20] Y. Shi, Z. Zhu, D. Miao, Y. Ding, Q. Mi, *ACS Energy Lett* **2024**, *9*, 1895.
[21] S. Shahbazi, M. Y. Li, A. Fathi, E. W. G. Diau, *ACS Energy Lett* **2020**, *5*, 2508.
[22] C. H. Kuan, Y. A. Ko, E. Wei-Guang Diau, *ACS Energy Lett* **2023**, *8*, 2423.
[23] C. C. Chen, Y. H. Chen, V. S. Nguyen, S. Y. Chen, M. C. Tsai, J. S. Chen, S. Y. Lin, T. C. Wei, C. Y. Yeh, *Adv. Energy Mater.* **2023**, *13*, 2300353.
[24] L. Ren, L. Liang, Z. Zhang, Z. Zhang, Q. Xiong, N. Zhao, Y. Yu, R. Scopelliti, P. Gao, *RSC Adv* **2021**, *11*, 3792.
[25] Y. Li, K. Yao, H. L. Yip, F. Z. Ding, Y. X. Xu, X. Li, Y. Chen, A. K. Y. Jen, *Adv. Funct. Mater.* **2014**, *24*, 3631.